Title

CD46-targeted theranostics for Positron Emission Tomography and 225Ac-Radiopharmaceutical Therapy of Multiple Myeloma

Journal

Clinical Cancer Research, 30(5)

ISSN

1078-0432

Authors

Wadhwa, Anju

Wang, Sinan

Patiño-Escobar, Bonell

et al.

Publication Date

2024-03-01

DOI

10.1158/1078-0432.ccr-23-2130

Peer reviewed

CD46-Targeted Theranostics for PET and ^{225}Ac-Radiopharmaceutical Therapy of Multiple Myeloma

Anju Wadhwa[1], Sinan Wang[1,2], Bonell Patiño-Escobar[3,4], Anil P. Bidkar[1], Kondapa Naidu Bobba[1], Emily Chan[3,4], Niranjan Meher[1], Scott Bidlingmaier[5], Yang Su[5], Suchi Dhrona[1], Huimin Geng[4], Vishesh Sarin[3,4], Henry F. VanBrocklin[1,3], David M. Wilson[1,3], Jiang He[6], Li Zhang[3,7], Veronica Steri[3], Sandy W. Wong[8], Thomas G. Martin[8], Youngho Seo[1,3], Bin Liu[3,5], Arun P. Wiita[3,4,9,10], and Robert R. Flavell[1,3,11]

ABSTRACT

Purpose: Multiple myeloma is a plasma cell malignancy with an unmet clinical need for improved imaging methods and therapeutics. Recently, we identified CD46 as an overexpressed therapeutic target in multiple myeloma and developed the antibody YS5, which targets a cancer-specific epitope on this protein. We further developed the CD46-targeting PET probe [^{89}Zr]Zr-DFO-YS5 for imaging and [^{225}Ac]Ac-DOTA-YS5 for radiopharmaceutical therapy of prostate cancer. These prior studies suggested the feasibility of the CD46 antigen as a theranostic target in multiple myeloma. Herein, we validate [^{89}Zr]Zr-DFO-YS5 for immunoPET imaging and [^{225}Ac]Ac-DOTA-YS5 for radiopharmaceutical therapy of multiple myeloma in murine models.

Experimental Design: *In vitro* saturation binding was performed using the CD46 expressing MM.1S multiple myeloma cell line. ImmunoPET imaging using [^{89}Zr]Zr-DFO-YS5 was performed in immunodeficient (NSG) mice bearing subcutaneous and systemic multiple myeloma xenografts. For radioligand therapy, [^{225}Ac]Ac-DOTA-YS5 was prepared, and both dose escalation and fractionated dose treatment studies were performed in mice bearing MM1.S-Luc systemic xenografts. Tumor burden was analyzed using BLI, and body weight and overall survival were recorded to assess antitumor effect and toxicity.

Results: [^{89}Zr]Zr-DFO-YS5 demonstrated high affinity for CD46 expressing MM.1S multiple myeloma cells (K_d = 16.3 nmol/L). *In vitro* assays in multiple myeloma cell lines demonstrated high binding, and bioinformatics analysis of human multiple myeloma samples revealed high CD46 expression. [^{89}Zr]Zr-DFO-YS5 PET/CT specifically detected multiple myeloma lesions in a variety of models, with low uptake in controls, including CD46 knockout (KO) mice or multiple myeloma mice using a nontargeted antibody. In the MM.1S systemic model, localization of uptake on PET imaging correlated well with the luciferase expression from tumor cells. A treatment study using [^{225}Ac]Ac-DOTA-YS5 in the MM.1S systemic model demonstrated a clear tumor volume and survival benefit in the treated groups.

Conclusions: Our study showed that the CD46-targeted probe [^{89}Zr]Zr-DFO-YS5 can successfully image CD46-expressing multiple myeloma xenografts in murine models, and [^{225}Ac]Ac-DOTA-YS5 can effectively inhibit the growth of multiple myeloma. These results demonstrate that CD46 is a promising theranostic target for multiple myeloma, with the potential for clinical translation.

Introduction

Multiple myeloma is the second most common hematologic malignancy among adults, with >33,000 new cases diagnosed per year in the United States (1). Multiple myeloma is a highly heterogeneous disease, and distinct subtypes of this disease can result in different outcomes and clinical–pathological features. Despite tremendous progress in multiple myeloma treatment in recent decades, there is no known cure (2). Patients typically endure cycles of initial response but subsequent resistance and relapse after treatment with different therapeutic agents (3). In particular, patients with extramedullary disease (i.e., myeloma tumor established outside of the typical location within the bone marrow) are considered high risk with no established treatment strategy (4). This indication in particular has an urgent need for novel therapeutic strategies. The current imaging approach for multiple myeloma includes radiographic skeletal surveys, whole-body low-dose CT, whole-body MRI, and 2-deoxy-2-[^{18}F]-fluorodeoxyglucose ([^{18}F]-FDG) PET (5, 6). These modalities have complementary roles, with MRI being highly sensitive for bone marrow disease, and [^{18}F]-FDG PET being most useful for detecting extramedullary disease as well as for assessing response to treatment (7, 8). However, [^{18}F]-FDG exhibits limitations including high background uptake in tissues like brain and bone marrow, false positives due to

[1]Department of Radiology and Biomedical Imaging, University of California, San Francisco, California. [2]School of Biomedical Engineering, ShanghaiTech University, Shanghai, China. [3]UCSF Helen Diller Family Comprehensive Cancer Center, San Francisco, California. [4]Department of Laboratory Medicine, University of California, San Francisco, California. [5]Department of Anesthesia, University of California, San Francisco, California. [6]Department of Radiology and Medical Imaging, University of Virginia, Charlottesville, Virginia. [7]Department of Medicine, Department of Epidemiology and Biostatistics, University of California, San Francisco, California. [8]Department of Medicine, Division of Hematology/Oncology, University of California, San Francisco, California. [9]Department of Bioengineering and Therapeutic Sciences, University of California, San Francisco, California. [10]Chan Zuckerberg Biohub, San Francisco, California. [11]Department of Pharmaceutical Chemistry, University of California, San Francisco, California.

Anju Wadhwa and Sinan Wang contributed equally to this work.

Corresponding Author: Robert R. Flavell, Department of Radiology and Biomedical Imaging, and Department of Pharmaceutical Chemistry, University of California, San Francisco, 185 Berry Street, San Francisco, CA 94143. E-mail: robert.flavell@ucsf.edu

Clin Cancer Res 2024;30:1009–21

doi: 10.1158/1078-0432.CCR-23-2130

Translational Relevance

There is an unmet clinical need for improved imaging methods for detecting multiple myeloma and improved treatments. Recently, we identified CD46 as an overexpressed therapeutic target in multiple myeloma and have successfully developed the antibody YS5, which specifically targets a cancer-specific epitope on this protein. Herein, we report the preclinical evaluation of CD46-directed theranostics in multiple myeloma. [^{89}Zr]Zr-DFO-YS5 was evaluated for immunoPET imaging of multiple myeloma in different murine models, which demonstrate specific, target-mediated imaging with a high tumor uptake. Further, we have performed radiopharmaceutical therapy with [^{225}Ac]Ac-DOTA-YS5 in a systemic model of multiple myeloma, with a marked reduction in tumor burden and improvement in overall survival. These results highlight the efficacy of CD46 targeted theranostics in multiple myeloma and strongly support future clinical translation.

inflammation or osteoarthritis, and false negatives due to low expression of hexokinase in some multiple myeloma lesions (9). Therefore, there is an unmet clinical need for improved imaging methods to detect multiple myeloma.

With the recent FDA approval of [^{177}Lu]Lu-DOTATATE (Lutathera) and [^{177}Lu]Lu-PSMA-617 (Pluvicto), theranostics promise to change the standard of care in multiple cancer types (10–12). The basic therapeutic strategy requires targets that are overexpressed in cancer cells but not in normal tissues. A key advantage of this approach is the paired utilization of molecular imaging (typically with PET) together with radiopharmaceutical therapy using analogous molecules. Studies using CXCR4 (13–15), CD38 (16–18), CD56 (19, 20), CD158 (21), or CD20 (22) as theranostic targets have shown success in multiple myeloma imaging and therapy in preclinical studies and in clinical trials. Of these theranostic targets, CXCR4 has attracted significant attention in both solid tumors and multiple myeloma, with great promise in clinical trials and preclinical models (23–25). In addition, clinical trials for radioimmunotherapy (RIT) with [^{111}In]In/[^{225}Ac]Ac-DOTA-Daratumumab targeting CD38 are ongoing (NCT053631111). However, despite these advances, none of these agents have yet risen to the standard of care, and there remains an unmet need for improved theranostic strategies for the imaging and treatment of multiple myeloma.

CD46 is a recently identified therapeutic target for multiple myeloma (26). It is located on chromosome 1q, which is commonly amplified in relapsed patients with multiple myeloma. In 2016, we reported that CD46 expression was markedly higher in multiple myeloma cells with 1q copy gain, a high-risk subtype of multiple myeloma, and identified a human monoclonal antibody (23AG2, aka YS5; ref. 26) binding to a tumor-selective CD46 epitope (27). We then developed an antibody–drug conjugate by conjugating auristatin derivatives [monomethyl auristatin F (MMAF) and monomethyl auristatin E (MMAE)] to YS5 and found strong *in vitro* and *in vivo* antitumor activity across multiple myeloma preclinical models (27). This MMAE-conjugated ADC (FOR46) is now in a multicenter phase I clinical trial for multiple myeloma (NCT03650491), as well as prostate cancer, with promising initial results reported (28). In parallel, we have successfully developed a CD46-targeting PET probe [^{89}Zr]Zr-DFO-YS5 for prostate cancer imaging with high sensitivity and validation in numerous preclinical models (29). A clinical trial of this imaging agent is now enrolling men with prostate cancer (NCT05245006). Similarly, we found promising therapeutic results in prostate cancer models, using the targeted alpha particle nanogenerator [^{225}Ac]Ac-DOTA-YS5 (30). Taken together, these results demonstrate great promise for the use of CD46-directed theranostics in multiple myeloma using the YS5 antibody as a platform.

Herein, we report the development and initial evaluation of CD46-directed theranostics in multiple myeloma. [^{89}Zr]Zr-DFO-YS5 was evaluated for immunoPET imaging of multiple myeloma in murine models, which demonstrates a key finding of specific, target-mediated imaging with a high tumoral uptake. Moreover, radiopharmaceutical therapy with [^{225}Ac]Ac-DOTA-YS5 was tested in a systemic model of multiple myeloma, with a marked reduction in tumor burden and improvement in overall survival. Taken together, these results demonstrate the efficacy of CD46 theranostics in multiple myeloma and strongly support future clinical translation.

Materials and Methods

General materials

The recombinant fully human CD46-targeted antibody, YS5, was generated from mammalian cell expression and purified as described previously (26). ^{89}Zr oxalate was purchased from 3D Imaging (Little Rock) and the Cyclotron Laboratory at the University of Wisconsin. ^{225}Ac was purchased from the Department of Energy Isotope Production Program and produced at Oak Ridge National Laboratory via the ^{229}Th generator route. p-Isothiocyanate-benzyl-DFO (Catalog No. B-705) and p-Isothiocyanate-benzyl-DOTA (Catalog No. B-205) were purchased from Macrocyclics, Inc. Native human IgG (Catalog No. ab91102) was purchased from Abcam. iTLC-SG (Catalog No. SG10001) was purchased from Agilent Technologies.

Antibody conjugation and radiolabeling

DFO-YS5, DFO-IgG, and [^{89}Zr]Zr-DFO-YS5 and [^{89}Zr]Zr-DFO-IgG were synthesized as reported previously (29). Conjugation of antibody YS5 as well as IgG with DOTA and further radiolabeling with $^{225}AcNO_3$ was carried out by following previously reported procedures (30). The dose calibrator details to measure the activity of the radioisotopes (^{89}Zr and ^{225}Ac) have been included in the Supplementary Materials and Methods.

Cell culture

MM.1S, RPMI8226, and AMO1 cell lines were obtained from the ATCC. The accession numbers for the MM1S, RPMI8226, and AMO1 cell lines are CRL-2974, CCL-155, and ACC 538, respectively. The ANBL6 cells were obtained from Dr. Diana Jelinek (Mayo Clinic; RRID:CVCL_5425). MM1.S cells, RPMI8226 cells, AMO1, and ANBL6 cells were maintained in RPMI1640 medium supplemented with 20% FBS, 100 U penicillin, and 100 μg/mL streptomycin in a humidified incubator at 37°C and 5% CO_2. ANBL6 cells were grown in RPMI1640 medium supplemented with 20% FBS, 100 U penicillin, 100 μg/mL streptomycin, and 2 ng/mL IL6 in a humidified incubator at 37°C and 5% CO_2 (31). Cell lines used in our studies were negative for mycoplasma contamination when tested with bioluminescence-based MycoAlert Mycoplasma Detection Kit in our UCSF cell culture lab.

Generation of luc+ cells

All cell lines MM.1S, RPMI8226, ANBL6, AMO1, and MM1.S CD46 (−/−) were all modified to stably express luciferase according to a previously established procedure and transduced with a lentiviral vector expressing mCherry fluorescent tag (32). Tumor burden was assessed through noninvasive bioluminescence.

Cas9 knockouts of MM.1S cells

Cas9 protein and sgRNA or scrambled sgRNA were mixed in a 1:1 molar ratio (Synthego Corporation) and incubated at 37°C for 10 to 15 minutes. MM.1S cells (1 million) were spun down and washed with PBS, resuspended in 20 μL of SF nucleofection/solution plus cas9/sgRNA mixture (SF Cell Line 4D-Nucleofector X Kit S; Lonza), and nucleofected using the DS-137 nucleofection program in Lonza 4D-Nucleofector. Eighty microliters of warm RPMI1640 media (Gibco) supplemented with 20% of FBS, GlutaMAX, and 100 U penicillin, 100 μg/mL streptomycin was plated into each well and incubated at 37°C for 15 minutes, then transferred to a 6-well to recover for 48 hours. Then, based on the surface expression by flow cytometry, negative clones were sorted using FACSARIA II flow cytometer (BD Biosciences). sgRNA sequences were obtained from the Brunello Library (33) as follows: CD46: AUUGUGGUGACA-AUUCAGUG; negative control, scrambled sgRNA#1 and #2 mod-sgRNA specified by Synthego Corporation.

Computational epigenetic analysis

Methods for computational epigenetic analysis to identify possible transcriptional regulators of CD46 have been included in the Supplementary Materials and Methods.

In vitro K_d measurement

The K_d value of [^{89}Zr]Zr-DFO-YS5 against CD46-expressing cell line MM.1S was determined by a saturation binding assay. An aliquot of 5×10^5 MM.1S cells was added to each of 18 0.5 mL centrifuge vials. The cells were centrifuged, and the supernatant was removed. The pellet was washed with PBS twice. Various concentrations (200 μL/vial, 0.0005–50 nmol/L, triplicate) of [^{89}Zr]Zr-DFO-YS5 in PBS containing 1% nonfat milk were added to cells. The cells were incubated with [^{89}Zr]Zr-DFO-YS5 containing buffer for 1 hour at 37°C. After that, the cells were centrifuged, and the supernatant was removed. The pellet was washed with PBS twice. The radioactivity bound to the cell pellet was counted using a Hidex gamma counter. K_d value and B_{max} were calculated by nonlinear regression, one site-specific binding using GraphPad Prism Software (GraphPad Software).

Flow cytometry

Cells were resuspended in FACS buffer (2% FBS in D-PBS) and stained with CD46 (BioLegend, clone MEM-258) and CD138 (BioLegend, clone DL-101) antibodies for 30 minutes at 4°C, washed, and then resuspended in FACS buffer. For experiments where live cell populations were analyzed by flow cytometry with anti CD46-YS5 antibody, cells were resuspended in 100 μL of FACS buffer, labeled with 0.5, 1, or 2 μg of YS5 antibody, incubated for 30 minutes at 4°C and then stained with AffiniPure F(ab′)$_2$ Fragment Goat Anti-Human IgG, Fc Fragment Specific (Jackson ImmunoResearch Laboratories Inc.) at 1:50 concentration as recommended per manufacturer, washed and resuspended in FACS buffer. Samples were analyzed using either a Cytoflex Flow Cytometer (Beckman Coulter) or FACSAria II flow cytometer (BD Biosciences). Data analysis was done using FlowJo software, v10.8.1, RRID:SCR_008520). Antibodies used were FITC anti-human CD46 Antibody (BioLegend 315304, RRID:AB_2291290; 0.013 nmol/L), APC anti-human CD138 (Syndecan-1) Antibody (BioLegend 352308, RRID:AB_10896946; 0.013 nmol/L), FITC Mouse IgG1, κ Isotype Ctrl Antibody (BioLegend 400108, RRID:AB_400108; 33 nmol/L), APC Mouse IgG1, κ Isotype Ctrl (BioLegend 981806; 0.013 nmol/L), and fluorescein (FITC)-conjugated AffiniPure F(ab′)$_2$ Fragment Goat Anti-Human IgG, Fc Fragment Specific (minimal cross-reaction to Bovine, Horse, and Mouse Serum Proteins; Jackson ImmunoResearch Laboratories Inc., 109–096–098; 100 nmol/L).

Cell binding assay

Cell numbers of MM.1S, RPMI8226, ANBL6, AMO1, or CD46-KO MM.1S were counted. Thirty million cells of each cell line were aliquoted to a 1.7 mL centrifuge vial (in triplicate). The cells were centrifuged at 1,000 revolutions per minute, and the supernatant was removed. The pellet was washed with PBS twice. Then 0.05 μCi [^{89}Zr]Zr-DFO-YS5 in 200 μL PBS (final antibody concentration of 3.125 nmol/L) containing 1% nonfat milk was added to each vial. The cells were incubated in this buffer for 1 hour at 37°C. The cells were centrifuged, and the supernatant was removed. The pellet was washed with PBS twice. The radioactivity of the cell pellet and 0.05 μCi [^{89}Zr]Zr-DFO-YS5 was counted using a Hidex Gamma Counter using a 480 to 558 keV counting window. Cell-associated activity percentage was calculated by cell pellet activity/0.05 μCi [^{89}Zr]Zr-DFO-YS5 activity.

Animal studies–xenograft models

All animal studies were conducted according to Institutional Animal Care and Use Committee–approved protocols at the University of California (AN194778). To generate the subcutaneous multiple myeloma xenograft models, a mixture of male and female NOD SCID gamma (NSG, stock 005557, The Jackson Laboratory) mice ages 4 to 8 weeks old were inoculated subcutaneously with 10 million MM1.S-Luc, RPMI8226-Luc, or ANBL6-Luc cells in a 1:1 mixture (v/v) of cells in PBS and Matrigel (Thermo Fischer Scientific, 08774391). To generate systemic multiple myeloma xenograft models (also called disseminated, or orthometastatic), 5×10^5 MM1.S-Luc or RPMI8226-Luc cells in PBS were injected intravenously into a cohort of male and female NSG mice ages 4 to 8 weeks old. Bioluminescence imaging (BLI) was used to monitor graft status (typically injected tumor cells established themselves in the bone marrow of the femur close to joints in 10 days). Mice were subjected to PET imaging followed by biodistribution analysis when the subcutaneous tumor reached a size of 200 to 500 mm^3 and in the systemic xenograft model when mice showed bioluminescence signal within a reference range of 1×10^6 to 6.06×10^6 p/sec/cm^2/sr.

In vivo [^{89}Zr]Zr-DFO-YS5 and [^{18}F]-FDG PET and [^{89}Zr]Zr-DFO-IgG imaging studies

Approximately 2 to 4 weeks after tumor implantation, animals with subcutaneous tumors reaching 200 to 500 mm^3 or systemic multiple myeloma xenograft showing bioluminescence signal within a reference range 1×10^6 to 6.06×10^6 p/sec/cm^2/sr were anesthetized by isoflurane inhalation. For [^{18}F]-FDG PET/CT imaging, 7.5 to 10 MBq [200–220 μCi] of [^{18}F]-FDG was administered ($n = 4$) and imaging methods were identical to those reported previously (34). For [^{89}Zr]Zr-DFO-YS5 PET imaging, 3.70 to 5.55 MBq [100–150 μCi, 10 μg/mouse ($n = 4$)] of [^{89}Zr]Zr-DFO-YS5 and 0.5 mg nonspecific binding IgG, essential to block the Fc receptor in NSG mice in saline, was (35) administered through the tail vein. The animals were imaged at 6 days post-injection for the subcutaneous model or 4 days post-injection for the systemic model with a 20-minute acquisition time by using microPET/CT (Inveon; Siemens Medical Solutions). PET imaging data were acquired in list mode and reconstructed using an iterative 2D OSEM reconstruction algorithm (for Inveon data) provided by the manufacturer. The resulting image data were then normalized to the administered activity to parameterize images in terms of %IA/mL. Imaging data were viewed and processed using open-source Amide

software. CT images were acquired following PET for 10 minutes, and the CT data were used for attenuation correction for PET reconstruction and anatomic reference.

To validate the specificity of the tracer for multiple myeloma tumor targeting, three control studies were performed. PET imaging was performed 6 days after co-injection of [^{89}Zr]Zr-DFO-YS5 [5.55–6.29 MBq (150–170 μCi) ($n = 5$)] and 0.5 mg IgG with a group of mice bearing subcutaneous CD46 knockout (KO) MM.1S tumors. In a second blocking control study, a group of mice with MM.1S was co-injected with 0.5 mg unlabeled YS5, 0.5 mg IgG, and [^{89}Zr]Zr-DFO-YS5 [5.92–7.03 MBq (160–190 μCi)], followed by PET imaging 6 days after injection. In a nontargeting antibody control study, a control mAb IgG (nonbinding control) was also radiolabeled with ^{89}Zr ([^{89}Zr]Zr-DFO-IgG) in the same process and the PET imaging of mice bearing MM.1S xenograft was recorded 6 days after injection followed by a biodistribution study. PET imaging of healthy nude and NSG mice was recorded with [^{89}Zr]Zr-DFO-IgG and biodistribution was also performed at 4 days after injection.

BLI

In vivo BLI was performed to monitor the tumor progression in mice injected with luciferase-expressing myeloma cells. D-Luciferin (LUCK-1G-Gold Biotechnology; 150 mg luciferin/kg body weight) dissolved in 100 μL PBS was intraperitoneally injected into mice, and they were allowed to move freely. After 9 minutes, mice were anesthetized and imaged using the IVIS 50 instrument. Images were acquired after 60 seconds of exposure time, and the intensity of the luciferase signal was quantified as radiance (photons/sec/cm^2/steradian) using an oval region of interest in Living Image 4.0 software.

For *ex vivo* bioluminescence studies, mice were injected intraperitoneally with D-Luciferin. After 5 minutes, mice were sacrificed, and organs were removed and plated in a petri dish. BLIs of the organs were acquired after 60 seconds of exposure time, and the intensity of the signal was calculated as described above.

Biodistribution studies

The tumor-bearing mice were sacrificed after PET/CT imaging. Blood was collected by cardiac puncture. For the subcutaneous model, major organs (bone, heart, kidney, large intestine, liver, lung, muscle, pancreas, small intestine, spleen, stomach, and subcutaneous tumor) were harvested. For the systemic model, bone marrow was extracted with some modifications in the previously established procedure (36). Briefly, a hole was created at the bottom of a 0.5 mL centrifuge tube using a needle. The femur was isolated from mice and was placed knee-end down in this 0.5 mL centrifuge tube. The 0.5 mL centrifuge tube was nested in a 1.7 mL centrifuge tube. Centrifuge the nested tubes at 10,000 rpm for 3 minutes. The bone marrow was collected in the 1.7 mL centrifuge tube. The organs collected were then weighed and counted in Hidex Gamma Counter in the 480 to 558 keV window. The percent injected activity per gram of tissue (%IA/g) was calculated by comparing with standards of known radioactivity.

Target binding fraction assay using magnetic beads

The target binding fraction assay for [^{225}Ac]Ac-DOTA-YS5 was performed according to the prior published protocol (37). The bead's activity, supernatant, and standard (10 ng of [^{225}Ac]Ac-DOTA-YS5) were measured on a Hidex gamma counter (energy window 25–2,000 keV). The binding fraction percentage was determined by calculating the bead's activity/standard.

Radioligand therapy for subcutaneous MM.1S tumor model

The detailed methodology for the radioligand therapy for the subcutaneous MM.1S tumor model has been included in the Supplementary Materials and Methods.

Radioligand therapy in the systemic MM.1S tumor model

Mice were administered 0.5 million MM.1S-Luc cells via the tail vein, and 7 days after injection, treatment was initiated. Mice were randomized to 6 treatment arms of $n = 8$ based on the average bioluminescence signal with a radiance value in between the range 1.40×10^4 p/sec/cm^2/sr to 7.00×10^6 p/sec/cm^2/sr. One mouse was kept separated from each group and used for the CD38 IHC. Treatment arms included a saline control, [^{225}Ac]Ac-DOTA-YS5 at dose levels of 0.0625 μCi or 0.125 μCi, or [^{225}Ac]Ac-DOTA-IgG at a dose level of 0.125 μCi. Additional fractionated dose arms of the study used administered activities of three fractions of 0.0625 μCi each and 0.125 μCi each of [^{225}Ac]Ac-DOTA-YS5 at days 0, 28, and 56, respectively. Fc blocking with 0.5 mg of cold native IgG was also performed in all the [^{225}Ac]Ac-DOTA-YS5 groups. Mice were monitored weekly via BLI as above. Body weight, activity, and overall mouse condition were monitored and analyzed at every third day. If body weight loss was ≥20% or mice demonstrated deteriorating conditions, including impaired motility or low body condition score (BSC < 2), they were euthanized. At day 120, the study was terminated with four mice alive. Overall survival was determined by Kaplan–Meier survival analysis. For the four surviving mice, animals were imaged with [^{89}Zr]Zr-DFO-YS5 PET/CT (as above), and tissues were harvested for toxicity analysis.

Necropsy and hematoxylin and eosin staining

The detailed methods for necropsy as well as for histology staining have been described in the Supplementary Materials and Methods.

IHC staining of CD138

The detailed methodology for IHC staining of CD138 has been added in the Supplementary Materials and Methods.

Statistical analysis

Data were analyzed using PRISM software (GraphPad; RRID: SCR_002798). The continuous variables were described by mean with SD and compared between two groups by using the unpaired and two-way ANOVA model. The survival data were estimated and described by the Kaplan–Meier method and were compared across groups with a log-rank sum test. Statistical significance was declared based on $P < 0.05$.

Data availability statement

The data presented in this study and in the Supplementary Information are available from the corresponding author upon request.

Results

CD46 is highly expressed in multiple myeloma, and can be detected using [^{89}Zr]DFO-YS5 in multiple myeloma cell lines *in vitro*

The binding affinity of [^{89}Zr]Zr-DFO-YS5 on the CD46-expressing multiple myeloma MM.1S cell line was verified through a saturation binding assay. Saturation binding analysis with [^{89}Zr]Zr-DFO-YS5 revealed a dissociation constant value, K_d of 16.5 ± 2.6 nmol/L, and a receptor density of 1.49×10^5 per cell in the MM.1S line (**Fig. 1A**). Further cell binding assays were performed to evaluate CD46 expression levels on different multiple myeloma cell lines. We found ANBL6

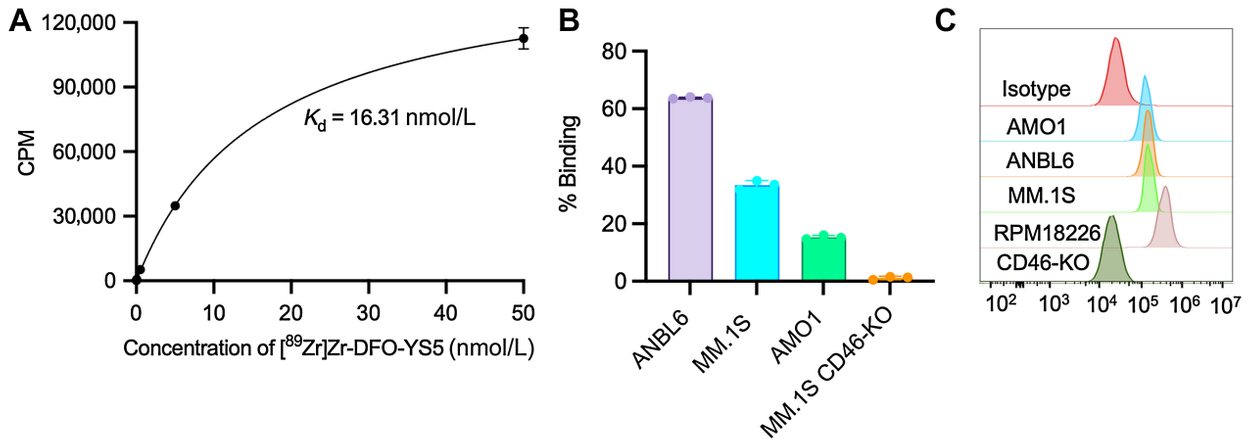

Figure 1.
[^{89}Zr]Zr-DFO-YS5 can detect CD46 expression in various multiple myeloma cell lines. **A,** K_d measurement of [^{89}Zr]Zr-DFO-YS5 on the MM.1S cell line ($n = 3$), determined by a saturation binding assay ($K_d = 16.31 \pm 2.6$ nmol/L) with a receptor density of 1.49×10^5 per cell. **B,** Cell binding assay to measure the percent cell-associated activity of [^{89}Zr]Zr-DFO-YS5 using different multiple myeloma cell lines ($n = 3$). **C,** Flow cytometry analysis of CD46 cell surface expression in various multiple myeloma cell lines ($n = 3$).

to have the highest cell binding percentage of [^{89}Zr]Zr-DFO-YS5, followed by MM.1S and AMO1. In contrast, the CD46 negative control cell line CD46-KO MM.1S did not demonstrate significant binding of the radiopharmaceutical (**Fig. 1B**). Similar results were found when the assay was performed using a smaller number of cells (30e6 cells vs. 1e6 cells), which again confirmed that ANBL6 has the highest cell binding percentage and CD46 expression, followed by RPMI8226, MM.1S, and AMO1, with very low binding in the CD46-KO MM.1S cell line (Supplementary Fig. S1). Flow cytometry was also performed to measure CD46 expression on different multiple myeloma cell lines, demonstrating strong surface expression of CD46 in AMO1, ANBL6, MM.1S, and RPMI8226 (**Fig. 1C**). We used a bioinformatics approach to evaluate the generality of these findings in human multiple myeloma. Leveraging myeloma patient tumor gene expression data in the Multiple Myeloma Research Foundation CoMMpass database (research.themmrf.org), we found a range of CD46 expression in primary tumors. Importantly all appeared positive for CD46 ($n = 776$, CoMMpass release IA13; Supplementary Fig. S2A). Given that CD46 surface antigen density may at least partially determine [^{89}Zr]DFO-YS5 binding, we further performed computational epigenetic analysis to identify possible transcriptional regulators of CD46. We identified transcription factors USF1 and XBP1 as potential positive regulators of CD46, and STAT4 as a potential negative regulator (Supplementary Fig. S2B–S2D). Together, these findings support the notion that CD46 is highly expressed in myeloma and can be recognized by [^{89}Zr]Zr-DFO-YS5.

μPET/CT imaging and biodistribution analysis of [^{89}Zr]Zr-DFO-YS5 in subcutaneous MM.1S tumor models reveal high tumor-to-background ratio imaging and CD46-targeted mediated uptake

Next, we evaluated the imaging properties of [^{89}Zr]Zr-DFO-YS5 in subcutaneous models ($n = 4$) of multiple myeloma using μPET/CT. The imaging study showed that [^{89}Zr]Zr-DFO-YS5 shows high uptake in the tumor and a relatively low background in other organs (**Fig. 2A**). A series of control experiments were performed to verify the specificity of [^{89}Zr]Zr-DFO-YS5 targeting CD46, including a blocking study ($n = 3$; **Fig. 2B**), imaging with a nonspecific binding ^{89}Zr-labeled antibody [^{89}Zr]Zr-DFO-IgG ($n = 4$; **Fig. 2C**), and imaging in CD46-knockout tumor model ($n = 5$; **Fig. 2D**). These three control studies showed comparatively low uptake in the tumor. The biodistribution studies showed that the tumor uptake of [^{89}Zr]Zr-DFO-YS5 was 17.57 ± 3.23% IA/g (Supplementary Tables S1 and S2) at 6 days after injection, significantly higher than the blocking group 8.51 ± 2.35% IA/g ($P < 0.0001$; Supplementary Tables S3 and S4), nonspecific binding ^{89}Zr-labeled antibody group [^{89}Zr]Zr-DFO-IgG 4.07 ± 0.66% IA/g ($P < 0.0001$; Supplementary Tables S5 and S6), and CD46-knockout MM.1S group 3.02 ± 0.85% IA/g ($P < 0.0001$; **Fig. 2E**; Supplementary Tables S7 and S8). These results demonstrated that [^{89}Zr]Zr-DFO-YS5 can specifically image CD46-positive multiple myeloma with high uptake in the tumor.

μPET/CT imaging and biodistribution analysis using [^{89}Zr]Zr-DFO-YS5 in subcutaneous RPMI8226 and ANBL6 multiple myeloma models reveals high tumoral uptake

Two additional multiple myeloma cell lines, RPMI8226 and ANBL6, were studied by PET imaging and biodistribution analysis. In RPMI8226 tumor models, PET imaging revealed that mice administered [^{89}Zr]Zr-DFO-YS5 ($n = 4$) showed high uptake (**Fig. 3A**). In contrast, mice administered [^{89}Zr]Zr-DFO-IgG ($n = 5$) showed low tumor uptake (**Fig. 3B**). The biodistribution studies were consistent with the imaging results. In the RPMI8226 model, the tumor uptake is 9.65 ± 1.43% IA/g (**Fig. 3C**; Supplementary Tables S9 and S10), higher than the nonspecific binding group 3.65 ± 0.77% IA/g ($P < 0.0001$; Supplementary Tables S11 and S12). Similarly, in the ANBL6 tumor model, mice administered [^{89}Zr]Zr-DFO-YS5 ($n = 4$) showed high uptake (**Fig. 3D**), whereas mice administered [^{89}Zr]Zr-DFO-IgG ($n = 5$) showed low tumor uptake (**Fig. 3E**). In the ANBL6 model, the tumor uptake is 7.47 ± 0.86% IA/g ($n = 4$; **Fig. 3F**; Supplementary Tables S13 and S14), higher than the control group 3.44 ± 0.76% IA/g ($n = 5$; $P = 0.0005$; Supplementary Tables S15 and S16).

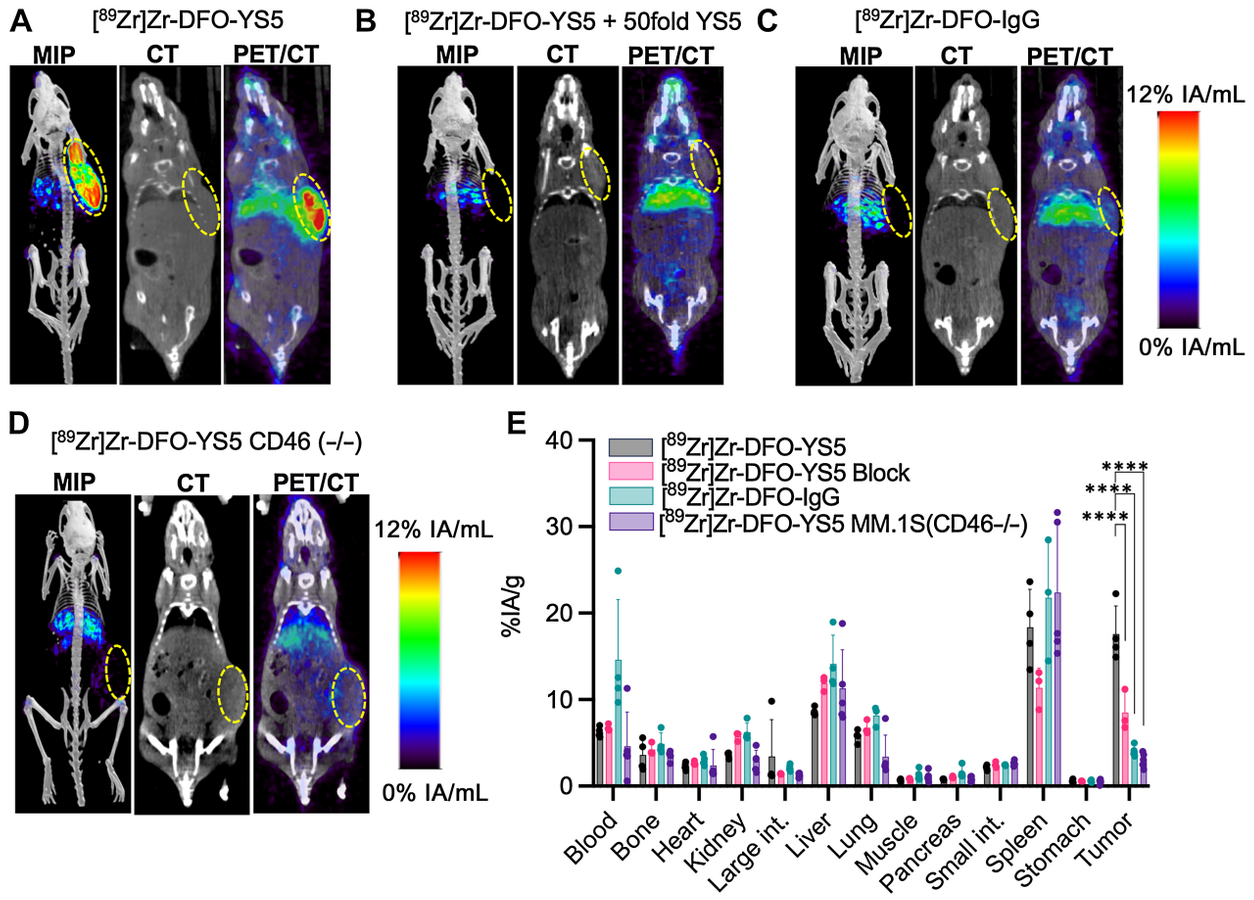

Figure 2.

[^{89}Zr]Zr-DFO-YS5 PET/CT can detect subcutaneous MM.1S xenografts *in vivo*. MIP and CT and μPET/CT fusion images of (**A**) [^{89}Zr]Zr-DFO-YS5 ($n = 4$), (**B**) 50-fold YS5 + [^{89}Zr]Zr-DFO-YS5 ($n = 3$), and (**C**) [^{89}Zr]Zr-DFO-IgG in NSG mice ($n = 4$) bearing subcutaneous MM.1S xenografts at 6 days post-injection. **D,** MIP and CT and μPET/CT fusion images of [^{89}Zr]Zr-DFO-YS5 in NSG mice bearing ($n = 5$) subcutaneous CD46-KO MM.1S (CD46−/−) xenograft at 6 days post-injection. **E,** Biodistribution of [^{89}Zr]Zr-DFO-YS5, [^{89}Zr]Zr-DFO-YS5 + 50-fold YS5, [^{89}Zr]Zr-DFO-IgG in NSG mice bearing subcutaneous MM.1S xenograft, and biodistribution of [^{89}Zr]Zr-DFO-YS5 in NSG mice bearing subcutaneous CD46-KO MM.1S (CD46−/−) xenograft at 6 days after injection. Two-way ANOVA *P* values are indicated as *, $P < 0.05$; **, $P < 0.01$; ***, $P < 0.001$; ****, $P < 0.0001$.

μPET/CT imaging and biodistribution of [^{18}F]-FDG in subcutaneous MM.1S, RPMI8226 and ANBL6 tumor models

We performed [^{18}F]-FDG μPET/CT, which is the standard of care for clinical staging and restaging of multiple myeloma. [^{18}F]-FDG imaging was performed and it revealed moderate uptake in the tumor in all three animal models ($n = 5$; **Fig. 4A–C**). The biodistribution study showed the uptake in MM.1S, RPMI8226, and ANBL6 xenografts were 5.76 ± 1.79% IA/g (Supplementary Tables S17 and S18), 4.90 ± 0.73% IA/g (Supplementary Tables S19 and S20), and 5.49 ± 0.70% IA/g (Supplementary Tables S21 and S22), respectively. In the other organs, the uptake in the brain, large intestine, and heart was higher than in the tumor (**Fig. 4D**).

μPET/CT imaging and biodistribution analysis of [^{89}Zr]Zr-DFO-YS5 and [^{18}F]-FDG in systemic multiple myeloma models

After demonstrating the imaging characteristics in subcutaneous xenograft models, we moved to evaluate the imaging performance of [^{89}Zr]Zr-DFO-YS5 ($n = 5$) in a more clinically relevant systemic model. At 10 days after administration of MM.1S-luc cells, multiple myeloma cells were mainly detected at the bone marrow, in some cases with a single tumor deposit and other cases with multiple deposits (**Fig. 5A**). One representative mouse monitored with BLI and [^{89}Zr]Zr-DFO-YS5 μPET/CT demonstrated a high signal in the femur bone marrow close to the knee (**Fig. 5A** and **B**). An *ex vivo* PET imaging and BLI study were performed after dissection to compare the uptake in different organs. The *ex vivo* BLI indicated heterogeneous bone marrow tumor involvement, with matching areas of [^{89}Zr]Zr-DFO-YS5 uptake ($n = 5$; **Fig. 5C**). Similarly, one representative mouse from the blocking group was monitored with BLI (**Fig. 5D**). For the blocking control study, mice ($n = 4$) were administered 50-fold cold YS5 together with [^{89}Zr]Zr-DFO-YS5, which reduced the uptake in bone marrow in the femur (**Fig. 5E**). The biodistribution studies in the systemic model showed that [^{89}Zr]Zr-DFO-YS5 had a higher uptake in the bone marrow 7.81 ± 2.74% IA/g at 4 days (Supplementary Tables S23 and S24) after injection than the blocked group 3.52 ± 0.96% IA/g (**Fig. 5F**; Supplementary Tables S25 and S26). Again, one representative mouse was monitored with BLI from the [^{18}F]-FDG injected cohort (**Fig. 5G**). [^{18}F]-FDG PET/CT imaging was performed, and it revealed a moderate uptake in the tumor ($n = 4$; **Fig. 5H**). The biodistribution study showed a similar pattern to the subcutaneous

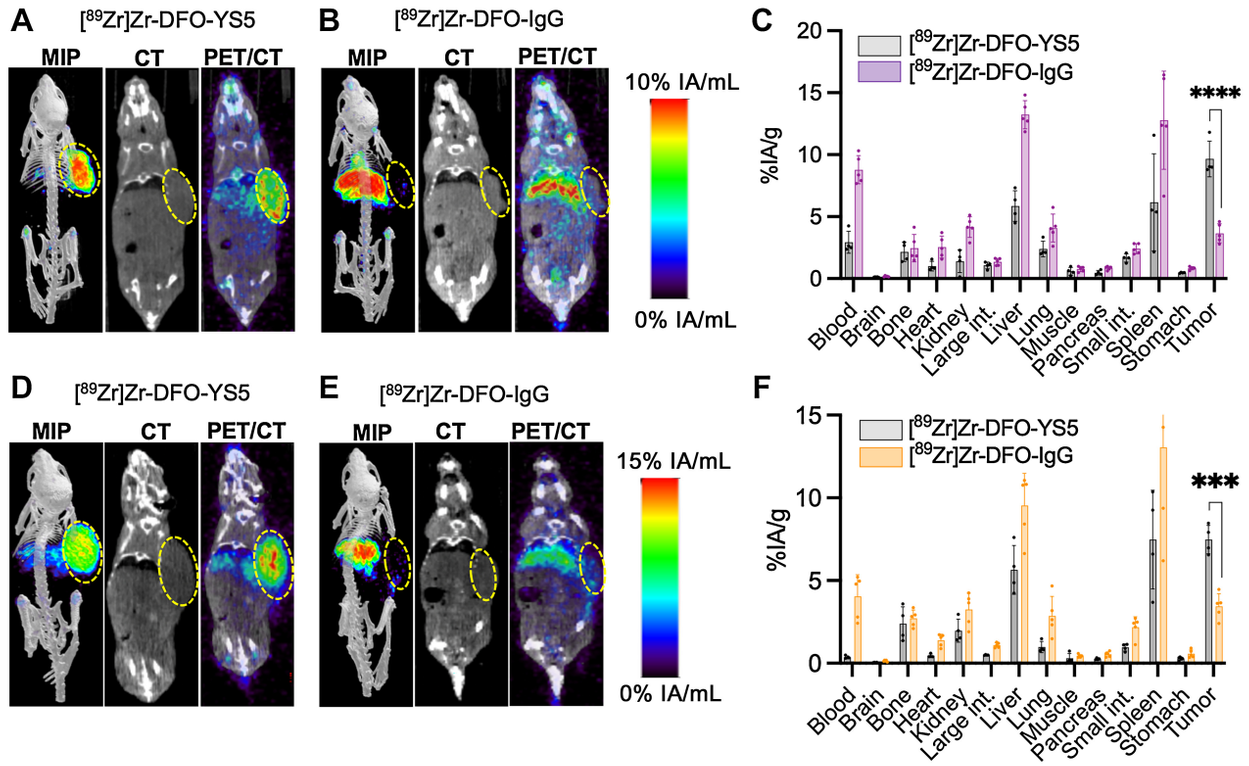

Figure 3.

[^{89}Zr]Zr-DFO-YS5 imaging and biodistribution in RPMI8226 and ANBL6 subcutaneous xenograft models. MIP and CT and μPET/CT fusion images of (**A**) [^{89}Zr]Zr-DFO-YS5 ($n = 4$) and (**B**) [^{89}Zr]Zr-DFO-IgG ($n = 5$) in NSG mice bearing subcutaneous RPMI8226 xenografts at 6 days after injection. **C,** Biodistribution of [^{89}Zr]Zr-DFO-YS5 and [^{89}Zr]Zr-DFO-IgG in NSG mice bearing subcutaneous RPMI8226 xenografts at 6 days after injection. MIP and CT and μPET/CT fusion images of (**D**) [^{89}Zr]Zr-DFO-YS5 ($n = 4$) and (**E**) [^{89}Zr]Zr-DFO-IgG ($n = 5$) in NSG mice bearing subcutaneous ANBL6 xenografts at 6 days after injection. **F,** Biodistribution of [^{89}Zr]Zr-DFO-YS5 and [^{89}Zr]Zr-DFO-IgG in NSG mice bearing subcutaneous ANBL6 xenografts at 6 days after injection. Two-way ANOVA *P* values are indicated as *, $P < 0.05$; **, $P < 0.01$; ***, $P < 0.001$; ****, $P < 0.0001$.

model, in which the brain, heart, and large intestine showed an uptake higher than the tumor (**Fig. 5I**; Supplementary Tables S27 and S28). These results demonstrate that both [^{18}F]-FDG PET/CT and [^{89}Zr]Zr-DFO-YS5 could detect the systemic tumor.

Similarly, the imaging capability of [^{89}Zr]Zr-DFO-YS5 was demonstrated in the RPMI8226 systemic multiple myeloma model. [^{18}F]-FDG imaging was also performed in the RPMI8226 systemic model. The BLI (Supplementary Fig. S3A) and μPET/CT imaging with [^{89}Zr]Zr-DFO-YS5 revealed high uptake in the femoral bone marrow (Supplementary Fig. S3B). [^{18}F]-FDG shows moderate uptake (Supplementary Fig. S3C and S3D). *Ex vivo* biodistribution also indicates that [^{89}Zr]Zr-DFO-YS5 showed high uptake in the bone marrow 11.57 ± 8.54% IA/g (Supplementary Fig. S3E; Supplementary Tables S29 and S30) and [^{18}F]-FDG showed 3.26 ± 2.71% IA/g (Supplementary Fig. S3F; Supplementary Tables S31 and S32).

Radiopharmaceutical therapy with [^{225}Ac]Ac-DOTA-YS5 in the MM.1S systemic tumor model demonstrates therapeutic efficacy, particularly in fractionated dosing regimens

Before moving on to the treatment study we performed a magnetic bead-based assay to determine the immunoreactivity of [^{225}Ac]Ac-DOTA-YS5 towards CD46. This study showed that the binding of [^{225}Ac]Ac-DOTA-YS5 was 91% ± 4% demonstrating preservation of immunoreactivity of radiolabeled antibody. The addition of 10-fold excess of cold YS5, and with no CD46 protein, significantly reduced bead binding to 13.66 ± 2% and 11.67 ± 0.5% (Supplementary Fig. S4). A treatment study was designed to evaluate the therapeutic efficacy of [^{225}Ac]Ac-DOTA-YS5 in the MM.1S systemic tumor model (schematized on **Fig. 6A** and presented in detail in Materials and Methods). The metastatic tumor study was informed by a pilot treatment study in subcutaneous xenograft mice which demonstrated dose-dependent antitumor efficacy (Supplementary Fig. S5), but also rapid tumor growth (Supplementary Fig. S5A), body weight loss (Supplementary Fig. S5B; particularly at the highest, 0.25 μCi dose level), and mortality in all arms (Supplementary Fig. S5C), suggesting that the more robust and clinically relevant metastatic model would be more suitable to evaluate therapeutic efficacy. In the metastatic tumor study, the control saline arm demonstrated continued tumor progression, with all mice reaching the endpoint at day 38 (**Fig. 6B**). In contrast, the [^{225}Ac]Ac-DOTA-YS5 treated groups demonstrated a dose-dependent decrease in tumor burden in both the single and fractionated dosing groups. No significant body weight loss (**Fig. 6C**) was observed other than one mouse in the 0.125 μCi [^{225}Ac]Ac-DOTA-YS5 fractionated dose arm, which had to be euthanized at day 110 post-administration due to body weight loss. One unexpected finding was also significant tumor burden reduction (demonstrated by BLI) in the 0.125 μCi dose of [^{225}Ac]Ac-DOTA-IgG, but also greatly enhanced toxicity as manifested by substantial body weight loss requiring euthanasia in 5 of 7 mice. This correlated with high blood retention and marrow uptake of the nontargeting therapeutic

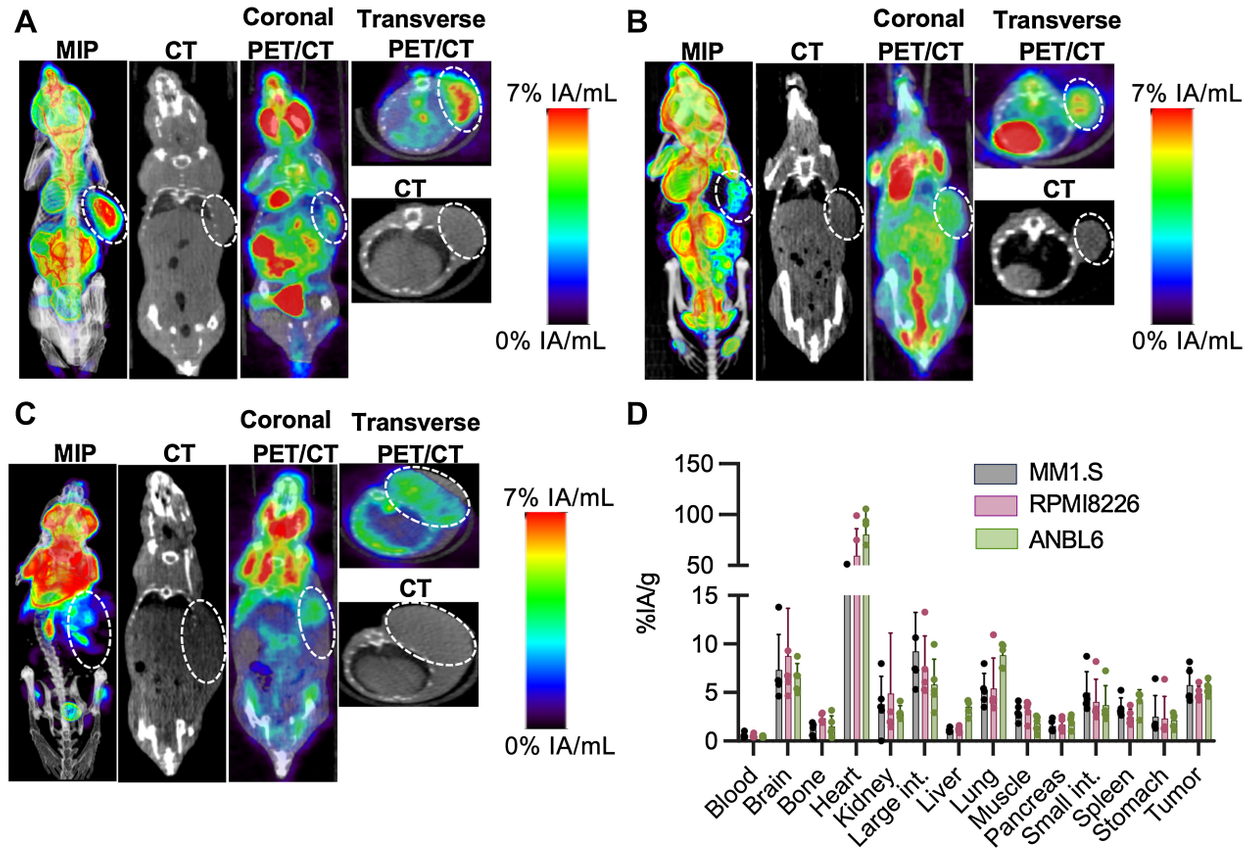

Figure 4.
[^{18}F]-FDG imaging and biodistribution in subcutaneous MM.1S, RPMI8226, and ANBL6 xenograft models. MIP and CT and μPET/CT fusion images of [^{18}F]-FDG (coronal and transverse posture) in (**A**) MM.1S (n = 5), (**B**) RPMI8226 (n = 5), and (**C**) ANBL6 (n = 5) subcutaneous xenografts at 1 hour after injection. **D,** Biodistribution of [^{18}F]-FDG in MM.1S, RPMI8226, and ANBL6 subcutaneous xenografts after μPET/CT imaging at 1 hour after injection.

radiopharmaceutical. This observation is corroborated by BLI (Supplementary Fig. S6A) and PET imaging (Supplementary Fig. S6B), demonstrating relatively high systemic uptake of [^{89}Zr]Zr-DFO-IgG in the MM.1S systemic model. The biodistribution study (Supplementary Fig. S6C) also confirmed the nonspecific uptake of [^{89}Zr]Zr-DFO-IgG in the MM1.S systemic model (Supplementary Tables S33 and S34). To confirm the nonspecific uptake of [^{89}Zr]Zr-DFO-IgG, we performed μPET/CT imaging and a biodistribution study with healthy nude mice and NSG healthy mice. The PET imaging (Supplementary Fig. S7A and S7B) and biodistribution (Supplementary Fig. S7C) showed high diffuse nonspecific uptake of [^{89}Zr]Zr-DFO-IgG in the bone marrow, spine, and spleen in NSG mice, which confirms that the accumulation of [^{89}Zr]Zr-DFO-IgG is strain-specific. These findings likely explain the therapeutic effect and weight loss in the cohort of mice injected with [^{225}Ac]Ac-DOTA-IgG.

The Kaplan–Meier curve showed that the median survival time of mice in the vehicle group was 38 days, whereas the median survival of the 0.0625 μCi and 0.125 μCi [^{225}Ac]Ac-DOTA-YS5-treated group was 59 days and 94 days, ($P < 0.05$) and ($P < 0.05$), respectively, and with three fractions of 0.0625 μCi each, the median survival was 91 ($P < 0.001$) and with three fractions of 0.125 μCi each the median survival was not defined (since 4 mice of 7 were still alive) during the end day of the treatment. In addition, the median survival with a 0.125 μCi dose of [^{225}Ac]Ac-DOTA-IgG was 45 days ($P = 0.25$; **Fig. 6D**). These data suggest that a fractionated regimen represents a promising method for treatment.

In addition, comparison with the saline group (**Fig. 6E**), 0.125 μCi [^{225}Ac]Ac-DOTA-YS5 injected group shows a decrease in CD138 expression in the femurs (BLI images of the corresponding mice Supplementary Fig. S8) 15 days after injection (**Fig. 6F**), which confirms tumor-targeted cell death and reduction in tumor burden.

The treatment study was completed at day 120 with four mice remaining in the 0.125 μCi fractionated dosing group. [^{89}Zr]Zr-DFO-YS5 PET/CT imaging of all surviving mice from the 0.125 μCi fractionated dose group at day 120 indicated that one mouse had tumor detected with BLI (Supplementary Fig. S9A) and [^{89}Zr]Zr-DFO-YS5 PET/CT imaging (Supplementary Fig. S9B), whereas one mouse had a focus of [^{89}Zr]Zr-DFO-YS5 PET/CT imaging found in the shoulder, with no matched BLI signal, which could represent an additional lesion (Supplementary Fig. S9C and S9D). In addition, two mice had no detectable tumor by either BLI or [^{89}Zr]Zr-DFO-YS5 PET/CT (Supplementary Fig. S9E, S9F, S9G, and S9H). These images suggest a potential for using [^{89}Zr]Zr-DFO-YS5 PET/CT to monitor the therapeutic effect of [^{225}Ac]Ac-DOTA-YS5, although these studies are limited by single time point analysis. Moreover, they do not support the loss of CD46 expression as a resistance mechanism following treatment in the mice with residual tumor. Histologic analysis of recovered tissues from this cohort demonstrated no detectable damage

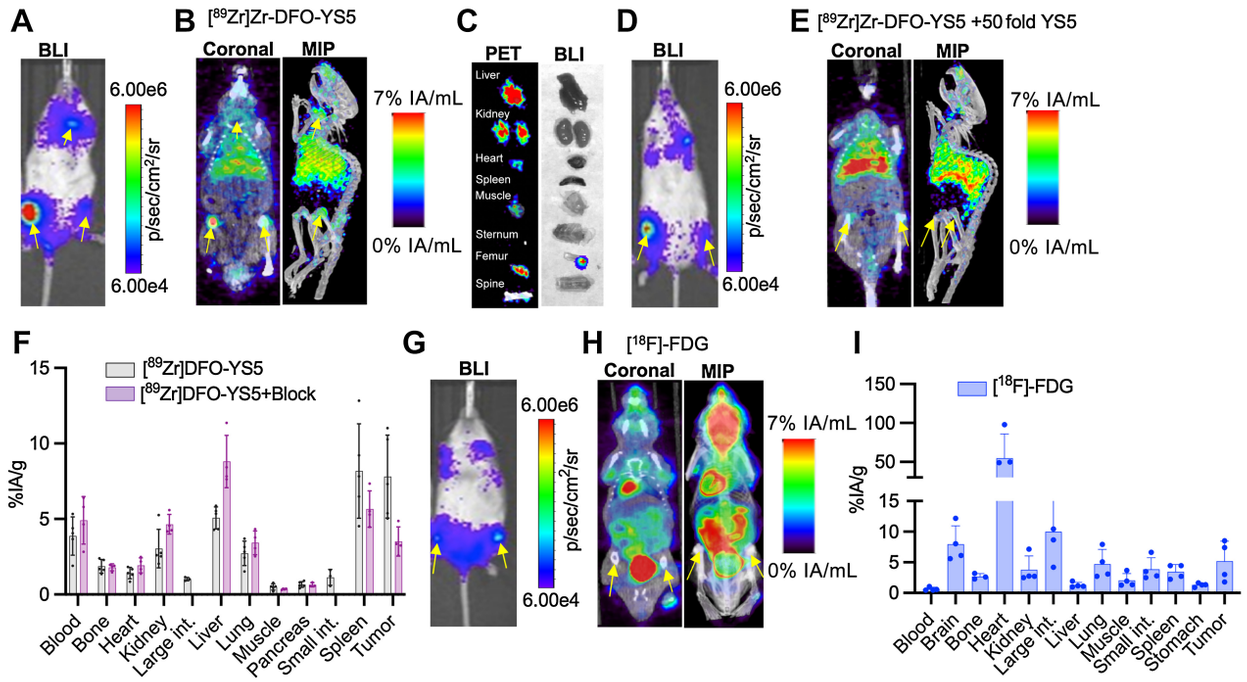

Figure 5.

[^{89}Zr]Zr-DFO-YS5 demonstrates favorable PET imaging characteristics in the MM.1S systemic tumor model. **A,** BLI of NSG mice bearing MM.1S systemic model revealed tumor was located in the femoral bone marrow. Sites of disease involvement are indicated with an arrow. **B,** Maximum intensity projections (MIP) and μPET/CT fusion images of [^{89}Zr]Zr-DFO-YS5 in NSG mice ($n = 5$) bearing systemic MM.1S xenograft at 4 days after injection revealed high tumor uptake in femur bone marrow, indicated by arrows. **C,** Correlation of *ex vivo* [^{89}Zr]Zr-DFO-YS5 PET images with bioluminescence, demonstrating matching regions of osseous PET uptake with tumor BLI signal. **D,** BLI of NSG mice bearing MM.1S systemic model. Sites of disease involvement are indicated with an arrow. **E,** MIP and μPET/CT of [^{89}Zr]Zr-DFO-YS5 with 50-fold block of cold YS5 in NSG mice ($n = 4$) bearing MM.1S systemic xenograft at 4 days after injection, demonstrating no detectable tumor uptake above background at the documented sites of tumor involvement (arrows). **F,** Biodistribution of [^{89}Zr]Zr-DFO-YS5, [^{89}Zr]Zr-DFO-YS5 with 50-fold block of cold YS5 in NSG mice bearing systemic MM.1S xenograft at 4 days after injection. **G,** BLI of NSG mice bearing MM.1S systemic model. Sites of disease involvement are indicated with an arrow. **H,** MIP and μPET/CT fusion images of [^{18}F]-FDG in NSG mice ($n = 4$) bearing MM.1S systemic xenograft at 1 hour after injection, demonstrating moderate tumor uptake. **I,** Biodistribution of [^{18}F]-FDG in NSG mice bearing systemic MM.1S xenograft.

to the liver, kidneys, bone marrow, heart, and spleen (Supplementary Fig. S10). Taken together, these demonstrate optimal outcomes at the fractionated dose level of 0.125 μCi of [^{225}Ac]Ac-DOTA-YS5 when compared against other arms.

Discussion

In this study, we have presented the systematic evaluation of CD46-directed PET imaging with [^{89}Zr]Zr-DFO-YS5 in a panel of preclinical models of multiple myeloma. Notably, high uptake was seen in all tested models including MM.1S, RPMI8226, and ANBL6. Relevant control studies including blocking, nonspecific IgG imaging, and CD46 knockout models demonstrate that the uptake of this agent is specific to the CD46 target, and not dominated by nonspecific accumulation. The apparent discrepancy in %ID/g when rank ordering ANBL6, RPMI8226, and MM.1S *in vitro* and *in vivo* may be due, at least in part, to the differences in the size of the tumors, as the total %ID per tumor (Supplementary Fig. S11) was 11.85 ± 1.06%, 8.38 ± 2.36%, 5.00 ± 0.31% for these cell lines, respectively. Additional features that could cause a discrepancy between the *in vitro* and *in vivo* binding and uptake of these radiopharmaceuticals could be variability in vascularity, tumor necrosis, or other features governing the enhanced permeability and retention effect. Our results demonstrated that [^{89}Zr]Zr-DFO-YS5 could effectively detect subcutaneous as well as systemic multiple myeloma tumors, although these results should be interpreted with caution as YS5 does not bind to endogenous mouse CD46. Taken together, these results support the further development of CD46 PET imaging with [^{89}Zr]Zr-DFO-YS5, and indeed we have recently opened a clinical multiple myeloma PET imaging trial (NCT05892393) using this agent, similar to our ongoing prostate cancer PET imaging clinical trial (NCT05245006).

Clinical translation of this PET agent is encouraged by important limitations in the existing methods for imaging multiple myeloma. Whole-body low-dose CT is preferred for detecting lytic bone lesions, and MRI is the method of choice for detecting bone marrow involvement in multiple myeloma (38). In addition, [^{18}F]-FDG PET/CT is considered the preferred imaging method to detect extramedullary multiple myeloma lesions and monitor metabolic treatment response to therapy. However, lesions with low metabolic rates may be undetectable with [^{18}F]-FDG (39, 40). In addition to [^{18}F]-FDG, new PET tracers such as L-methyl-[^{11}C]-methionine (MET) have been emerging as an imaging agent that targets different metabolic pathways (41).

We propose that CD46-directed PET imaging with [^{89}Zr]Zr-DFO-YS5 demonstrates promise for clinical evaluation, as currently being investigated for other tracers such as those directed against CD38, CXCR4, and others (42–45). A potential advantage of [^{89}Zr]Zr-DFO-YS5 compared with previously published agents is the tumor-specific CD46 epitope recognized by YS5 (27); all other explored targets are

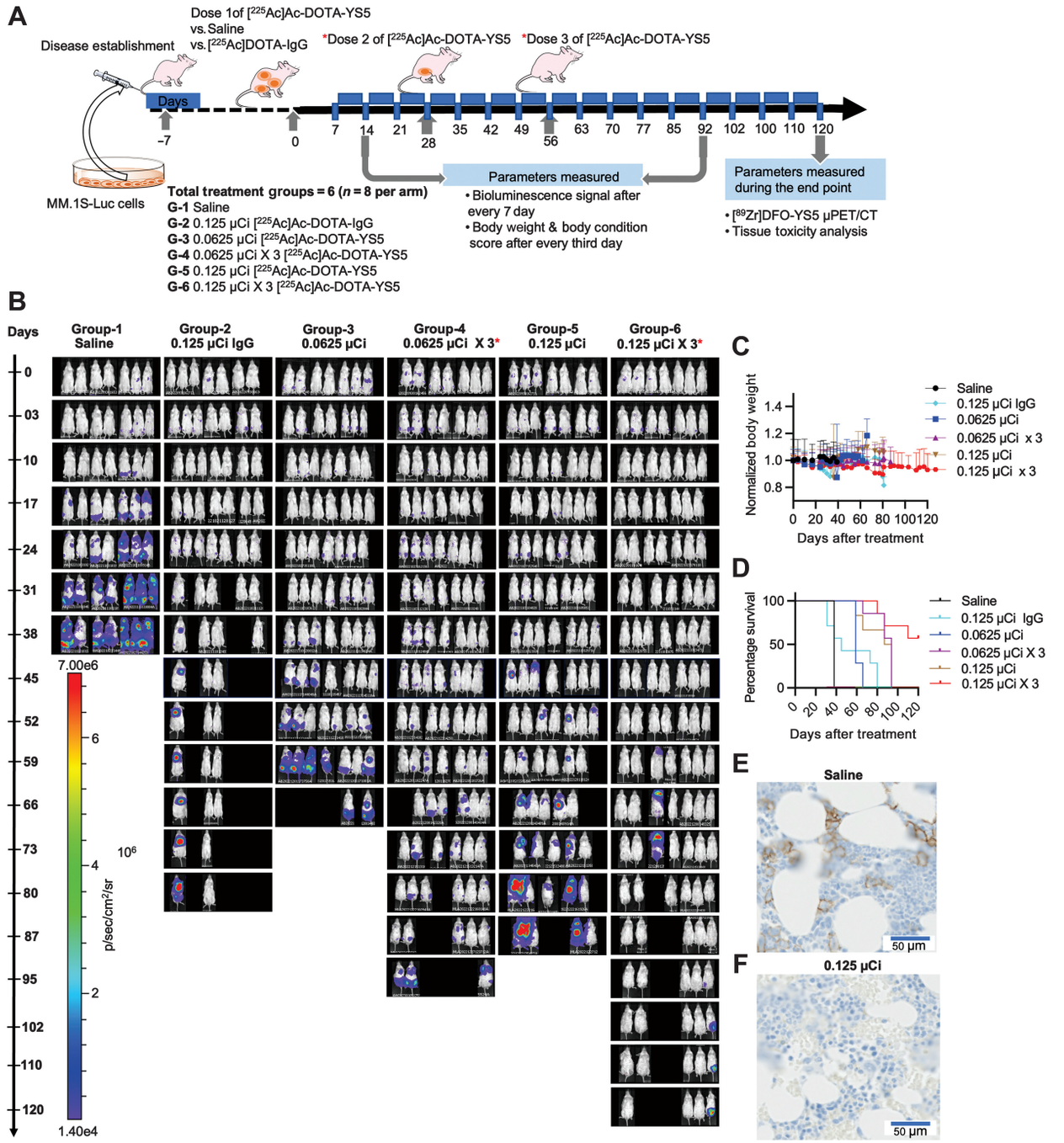

Figure 6.
[225Ac]Ac-DOTA-YS5 is an effective treatment for multiple myeloma in the MM.1S metastatic model. **A,** Schematic for therapeutic study. **B,** Serial BLI imaging indicates reduced tumor burden in the treatment groups (ventral view; $n = 8$). **C**, Body weight measurements in control and treatment groups. **D,** Kaplan–Meier curve demonstrates dose-dependent improvement in overall survival in the treatment arms. **E,** CD138 expressing cells in femurs in mice from the control group ($n = 1$) treated with saline after 15 days (**F**) decrease in CD138 expressing cells in femurs in mice treated with 0.125 μCi ($n = 1$) of [225Ac]Ac-DOTA-YS5 after 15 days, confirming tumor-targeted cell death and reduction in tumor burden.

expressed widely on other cell types in addition to multiple myeloma plasma cells, giving scope for false-positive results (46). In addition, CD38 antigen density can be significantly decreased in patients who previously received anti-CD38 mAb therapy (47), a standard part of current myeloma regimens (48, 49). Given the important limitations of the standard of care methods outlined above, there is great promise for the development of new molecular imaging and theranostic technologies such as [89Zr]Zr-DFO-YS5 PET in multiple myeloma. Our

imaging results demonstrate the feasibility of clinical translation of CD46-directed PET imaging in patients with multiple myeloma.

In multiple myeloma, radiopharmaceutical therapies demonstrate significant promise. In particular, several ongoing clinical studies are investigating the efficacy of ^{225}Ac-radioimmunoconjugates in a variety of cancers, including prostate cancer and acute myeloid leukemia (50–54). Both clinical and preclinical studies have shown efficacious results for daratumumab, which targets the CD38 protein in multiple myeloma cells. However, not all patients respond to daratumumab therapy (55). One limitation of current radioligand therapy strategies in multiple myeloma is the associated damage to the bone marrow and the need for associated stem cell transplantation. Because CD46 has low expression on normal marrow progenitor cells, targeting this antigen may avoid this complication in clinical studies. In addition, alpha particle-based radioligand therapy can kill malignant bone marrow cells with high-energy linear transfer and minimal effect on normal BM cells (56). Therefore, CD46-targeted radiopharmaceutical therapy with [^{225}Ac]Ac-DOTA-YS5 has the potential for reduced bone marrow toxicity in future clinical study.

Recently, Dawickki and colleagues conjugated daratumumab with ^{225}Ac and demonstrated a strong antitumor effect of [^{225}Ac]Ac-daratumumab against CD38-positive multiple myeloma tumors and clinical trial for this agent has been opened (NCT053631111; ref. 16). Similarly, treatment with [^{225}Ac]Ac-DOTA-YS5 demonstrated favorable outcomes in the MM.1S model. In particular, a fractionated dosing scheme using three fractions consisting of 0.125 μCi each substantially prolonged overall survival and reduced tumor burden compared with other groups (**Fig. 6**). Poor treatment outcomes were observed during treatment with [^{225}Ac]Ac-DOTA-IgG, which is due to nonspecific uptake of the radiotracer in the bone marrow which leads to toxicity (more than 20% body weight loss in most of the mice of this cohort). These data suggest that CD46-targeted radioligand therapy using [^{225}Ac]Ac-DOTA-YS5 is a promising strategy for the treatment of multiple myeloma. This is further supported by encouraging results from the phase I trial of CD46 ADC, and FOR46, in relapsed/refractory patients with multiple myeloma. In this study, patients had an overall response rate of 33% among 9 patients treated at dose levels ≥1.8 mg/kg (28).

There are important limitations related to this study which merit discussion. First, the mouse models employed in this study do not express human CD46, therefore potentially underestimating background radiopharmaceutical distribution. However, normal tissue IHC data demonstrate relatively low YS5 binding in normal human tissues expressing CD46 (26, 57), at least partially mitigating this concern. Another limitation of our study is that we have not performed IHC in the subcutaneous tumor sections (MM.1S, ANBL6, and RPMI8226), which could provide additional information about CD46 expression in different tumor models. In addition, our ^{225}Ac treatment studies were performed in the NSG mouse model due to our prior experience in growing the sensitive multiple myeloma cells in this strain. However, it is well known that NSG mice are more sensitive to radiation due to their highly suppressed DNA damage repair (58). Therefore, the toxicity of the therapy may be accentuated compared with other mouse models, potentially reducing the therapeutic efficacy and overall survival results compared with which might be obtained otherwise. However, this criticism is tempered by the promising overall therapeutic results in the fractionated regimen group, as well as the relative lack of toxicity observed. Finally, the [^{225}Ac]Ac-DOTA-YS5 agent utilized in this study requires a relatively high chelator-to-antibody ratio, potentially blunting therapeutic efficacy. This final limitation could be addressed by using more effective chelators such as Macropa, now underway in our laboratories (59, 60).

This study builds upon prior and ongoing work in our laboratories on the development of CD46 theranostics. As CD46 is a cancer antigen, which is widely expressed in many other malignancies, this suggests the potential for CD46 PET imaging and radiopharmaceutical therapy not only in multiple myeloma but also in other malignancies. This possibility will be tested in our clinical trial of [^{89}Zr]Zr-DFO-YS5 PET imaging in patients with multiple myeloma.

Conclusion

In this study, "[^{89}Zr]Zr-DFO-YS5 was tested as a CD46-targeted immunoPET imaging probe for MM" in different murine models, with higher tumor uptake and lower background than [^{18}F]-FDG. A YS5-based therapeutic agent, [^{225}Ac]Ac-DOTA-YS5, was also successfully prepared, and demonstrated effective antitumor treatment. Overall, [^{89}Zr]Zr-DFO-YS5 shows great potential for clinical translation as an imaging agent and theranostic companion biomarker, and [^{225}Ac]Ac-DOTA-YS5 shows promising results for further development as a multiple myeloma treatment.

Authors' Disclosures

B. Patiño-Escobar reports grants from the Multiple Myeloma Research Foundation (MMRF) during the conduct of the study. S. Bidlingmaier reports grants from NIH during the conduct of the study and has a patent for WO2016040683A1 issued, licensed, and with royalties paid from Fortis. Y. Su reports grants from NIH during the conduct of the study and has patents for WO2016040683A1 and WO2018089807 issued. H.F. VanBrocklin reports grants from NIH and the U.S. Department of Defense CDMRP during the conduct of the study. J. He reports grants from NCI during the conduct of the study and holds equity in Molecular Imaging and Therapeutics, Inc., which was converted to equity of Fortis Therapeutics, which licensed intellectual properties from the University of California. L. Zhang reports personal fees from Smith-Kettlewell Eye Research Institute outside the submitted work. S.W. Wong reports grants from Fortis, Bristol Myers Squibb, Johnson & Johnson, Alexion, and GSK as well as personal fees from Pfizer outside the submitted work. Y. Seo holds equity of Molecular Imaging and Therapeutics, Inc., which was converted to equity of Fortis Therapeutics, which licensed intellectual properties from the University of California. B. Liu reports grants from NIH during the conduct of the study; has patents for WO2016040683A1, US15390378, and WO2018089807 issued, licensed, and with royalties paid from Fortis; and reports being founder, board member, and shareholder of Fortis Therapeutics, Inc. A.P. Wiita reports other support from Sanofi outside the submitted work. R.R. Flavell reports grants from NIH/NCI, U.S. Department of Defense/CDMRP, and Stephen and Nancy Grand Multiple Myeloma Translational Initiative during the conduct of the study as well as grants from Fukushima SiC outside the submitted work; in addition, R.R. Flavell has a patent for patent application no. 63/344,537 pending. No disclosures were reported by the other authors.

Authors' Contributions

A. Wadhwa: Conceptualization, resources, data curation, software, formal analysis, visualization, methodology, writing–original draft, writing–review and editing. **S. Wang:** Conceptualization, resources, data curation, software, formal analysis, visualization, methodology, project administration, writing–review and editing. **B. Patiño-Escobar:** Conceptualization, resources, software. **A.P. Bidkar:** Data curation, formal analysis. **K.N. Bobba:** Data curation, methodology. **E. Chan:** Resources, data curation. **N. Meher:** Data curation, formal analysis. **S. Bidlingmaier:** Conceptualization, resources, methodology. **Y. Su:** Resources, formal analysis. **S. Dhrona:** Data curation, formal analysis. **H. Geng:** Resources, software. **V. Sarin:** Resources, software. **H.F. VanBrocklin:** Conceptualization, data curation, software, formal analysis, validation, methodology. **D.M. Wilson:** Conceptualization, resources, formal analysis, supervision, writing–review and editing. **J. He:** Conceptualization, resources, validation, investigation. **L. Zhang:** Data curation, formal analysis, visualization. **V. Steri:** Resources, software. **S.W. Wong:** Conceptualization, validation, investigation. **T.G. Martin:** Conceptualization, resources. **Y. Seo:** Conceptualization, data curation, software, supervision, methodology. **B. Liu:** Conceptualization, formal analysis, validation, visualization, methodology. **A.P. Wiita:** Conceptualization,

resources, data curation, software, supervision, funding acquisition, visualization, methodology. **R.R. Flavell:** Conceptualization, data curation, formal analysis, supervision, funding acquisition, validation, investigation, visualization, writing–original draft, project administration, writing–review and editing.

Acknowledgments

Robert R. Flavell and Arun Wiita acknowledge funding from Stephen and Nancy Grand Multiple Myeloma Translational Initiative and R01CA271606. ^{225}Ac was supplied by the U.S. Department of Energy Isotope Program. Histology staining procedures were performed by Histology and Biomarker Core, University of California San Francisco. The study was also supported in part by P30CA082103.

Note

Supplementary data for this article are available at Clinical Cancer Research Online (http://clincancerres.aacrjournals.org/).

Received July 17, 2023; revised September 26, 2023; accepted December 13, 2023; published first December 18, 2023.

References

1. Siegel RL, Miller KD, Fuchs HE, Jemal A. Cancer statistics, 2022. A Cancer Journal for Clinicians. CA Cancer J Clin 2022;72:7–33.
2. Vij R, Fowler KJ, Shokeen M. New approaches to molecular imaging of multiple myeloma. J Nucl Med 2016;57:1–4.
3. Rajkumar SV. Multiple myeloma: 2020 update on diagnosis, risk-stratification, and management. Am J Hematol 2020;95:548–67.
4. Bhutani M, Foureau DM, Atrash S, Voorhees PM, Usmani SZ. Extramedullary multiple myeloma. Leukemia 2020;34:1–20.
5. Heider M, Nickel K, Högner M, Bassermann F. Multiple myeloma: molecular pathogenesis and disease evolution. Oncology Research and Treatment 2021;44: 672–81.
6. Fonseca R, San Miguel J. Prognostic factors and staging in multiple myeloma. Hematol Oncol Clin North Am 2007;21:1115–40.
7. de Mel S, Lim SH, Tung ML, Chng W-J. Implications of heterogeneity in multiple myeloma. Biomed Res Int 2014;2014:1–12.
8. Zamagni E, Tacchetti P, Cavo M. Imaging in multiple myeloma: How? When? Blood 2019;133:644–51.
9. Matteucci F, Paganelli G, Martinelli G, Cerchione C. PET/CT in multiple myeloma: beyond FDG. Front Oncol. 2021;10:622501.
10. Strosberg J, El-Haddad G, Wolin E, Hendifar A, Yao J, Chasen B, et al. Phase 3 trial of ^{177}Lu-Dotatate for midgut neuroendocrine tumors. N Engl J Med 2017; 376:125–35.
11. Sartor AO, Morris MJ, Messman R, Krause BJ. VISION: an international, prospective, open-label, multicenter, randomized phase III study of ^{177}Lu-PSMA-617 in the treatment of patients with progressive PSMA-positive metastatic castration-resistant prostate cancer (mCRPC). Am Soc Clin Oncol 2021; 385:1091–103.
12. Jadvar H, Chen X, Cai W, Mahmood U. Radiotheranostics in cancer diagnosis and management. Radiology 2018;286:388–400.
13. Lapa C, Schreder M, Schirbel A, Samnick S, Kortüm KM, Herrmann K, et al. [^{68}Ga]Pentixafor-PET/CT for imaging of chemokine receptor CXCR4 expression in multiple myeloma—Comparison to [^{18}F]-FDG and laboratory values. Theranostics 2017;7:205–12.
14. Pan Q, Cao X, Luo Y, Li J, Feng J, Li F. Chemokine receptor-4 targeted PET/CT with ^{68}Ga-Pentixafor in assessment of newly diagnosed multiple myeloma: comparison to [^{18}F]-FDG PET/CT. Eur J Nucl Med Mol Imaging 2020;47: 537–46.
15. Herrmann K, Schottelius M, Lapa C, Osl T, Poschenrieder A, Hänscheid H, et al. First-in-human experience of CXCR4-directed endoradiotherapy with ^{177}Lu- and ^{90}Y-labeled pentixather in advanced-stage multiple myeloma with extensive intra-and extramedullary disease. J Nucl Med 2016;57: 248–51.
16. Dawicki W, Allen KJH, Jiao R, Malo ME, Helal M, Berger MS, et al. Daratumumab-^{225}Actinium conjugate demonstrates greatly enhanced antitumor activity against experimental multiple myeloma tumors. Oncoimmunology 2019;8: 1607673.
17. Ghai A, Maji D, Cho N, Chanswangphuwana C, Rettig M, Shen D, et al. Preclinical development of CD38-targeted [^{89}Zr] Zr-DFO-daratumumab for imaging multiple myeloma. J Nucl Med 2018;59:216–22.
18. Herrero Alvarez N, Michel AL, Viray TD, Mayerhoefer ME, Lewis JS. ^{89}Zr-DFO-isatuximab for CD38-targeted immunoPET imaging of multiple myeloma and lymphomas. ACS Omega 2023;25:22486–95.
19. Cottini F, Rodriguez J, Hughes T, Sharma N, Guo L, Lozanski G, et al. Redefining CD56 as a biomarker and therapeutic target in multiple myeloma. Mol Cancer Res 2022;20:1083–95.
20. Benjamin R, Condomines M, Gunset G, Sadelain M. CD56 targeted chimeric antigen receptors for immunotherapy of multiple myeloma. Cancer Res 2012;72: 3499.
21. Wolniak KL, Goolsby CL, Chen Y-H, Chenn A, Singhal S, Mehta J, et al. Expansion of a clonal CD8+ CD57+ large granular lymphocyte population after autologous stem cell transplant in multiple myeloma. Am J Clin Pathol 2013;139: 231–41.
22. Longtine MS, Shim K, Hoegger MJ, Abou DS, Thorek DLJ, Wahl RL. Cure of disseminated human lymphoma with [^{225}Ac] Ac-Ofatumumab in a preclinical model. J Nucl Med 2023;64:924–31.
23. Shekhawat AS, Singh B, Malhotra P, Watts A, Basher R, Kaur H, et al. Imaging CXCR4 receptors expression for staging multiple myeloma by using ^{68}Ga-Pentixafor PET/CT: comparison with ^{18}F-FDG PET/CT. Br J Radiol 2022;95: 20211272.
24. Buck AK, Serfling SE, Lindner T, Hänscheid H, Schirbel A, Hahner S, et al. CXCR4-targeted theranostics in oncology. Eur J Nucl Med Mol Imaging 2022;49: 4133–44.
25. Buck AK, Haug A, Dreher N, Lambertini A, Higuchi T, Lapa C, et al. Imaging of CXC motif chemokine receptor 4 expression in 690 patients with solid or hematologic neoplasms using ^{68}Ga-pentixafor PET. J Nucl Med 2022;63: 1687–92.
26. Sherbenou DW, Aftab BT, Su Y, Behrens CR, Wiita A, Logan AC, et al. Antibody-drug conjugate targeting CD46 eliminates multiple myeloma cells. J Clin Invest 2016;126:4640–53.
27. Su Y, Liu Y, Behrens CR, Bidlingmaier S, Lee N-K, Aggarwal R, et al. Targeting CD46 for both adenocarcinoma and neuroendocrine prostate cancer. JCI Insight 2018;3:E121497.
28. Wong S, Imus P, Mark T, Kaufman J, Imus A, Zonder JA, et al. P-225: a first-in-human study of FOR46 in patients with triple refractory multiple myeloma. Clin Lymphoma Myeloma Leuk 2021;21:S164.
29. Wang S, Li J, Hua J, Su Y, Beckford-Vera DR, Zhao W, et al. Molecular imaging of prostate cancer targeting CD46 using immunoPET. Clin Cancer Res 2021;27: 1305–15.
30. Bidkar AP, Wang S, Bobba KN, Chan E, Bidlingmaier S, Egusa EA, et al. Treatment of prostate cancer with CD46-targeted ^{225}Ac alpha particle radioimmunotherapy. Clin Cancer Res 2023;29:1916–28.
31. Sarin V, Yu K, Ferguson ID, Gugliemini O, Nix MA, Sirota M, et al. Evaluating the efficacy of multiple myeloma cell lines as models for patient tumors via transcriptomic correlation analysis. Leukemia 2020;6:2754–65.
32. Nix MA, Mandal K, Geng H, Paranjape N, Lin Y-HT, Rivera JM, et al. Surface proteomics reveals CD72 as a target for in vitro–evolved nanobody-based CAR-T cells in KMT2A/MLL1-rearranged B-ALL. Cancer Discov 2021;11: 2032–49.
33. Doench JG, Fusi N, Sullender M, Hegde M, Vaimberg EW, Donovan KF, et al. Optimized sgRNA design to maximize activity and minimize off-target effects of CRISPR-Cas9. Nat Biotechnol 2016;34:184–91.
34. Flavell RR, Truillet C, Regan MK, Ganguly T, Blecha JE, Kurhanewicz J, et al. Caged [^{18}F]-FDG glycosylamines for imaging acidic tumor microenvironments using positron emission tomography. Bioconjug Chem 2016, ACS. 27:170–8.
35. Sharma SK, Chow A, Monette S, Vivier D, Pourat J, Edwards KJ, et al. Fc-mediated anomalous biodistribution of therapeutic antibodies in immunodeficient mouse models. Cancer Res 2018;78:1820–32.
36. Smith AO, Adzraku SY, Ju W, Qiao J, Xu K, Zeng L. A novel strategy for isolation of mice bone marrow endothelial cells (BMECs). Stem Cell Res Ther 2021;12: 267.

37. Sharma SK, Lyashchenko SK, Park HA, Pillarsetty N, Roux Y, Wu J, et al. A rapid bead-based radioligand binding assay for the determination of target-binding fraction and quality control of radiopharmaceuticals. Nucl Med Biol 2019;71:32–38.
38. Garderet L, Kharroubi-Lakouas D, Roos Weil D, Jacque N, Ouarab MO, Martino S, et al. The role of PET-MRI in multiple myeloma patients. Blood 2020;136:12.
39. Cavo M, Terpos E, Nanni C, Moreau P, Lentzsch S, Zweegman S, et al. Role of ^{18}F-FDG PET/CT in the diagnosis and management of multiple myeloma and other plasma cell disorders: a consensus statement by the International Myeloma Working Group. Lancet Oncol 2017;18:E206–17.
40. Rasche L, Angtuaco E, McDonald JE, Buros A, Stein C, Pawlyn C, et al. Low expression of hexokinase-2 is associated with false-negative FDG–positron emission tomography in multiple myeloma. Blood 2017;130:30–34.
41. Morales-Lozano MI, Viering O, Samnick S, Rodriguez-Otero P, Buck AK, Marcos-Jubilar M, et al. [^{18}F]-FDG and [^{11}C]-Methionine PET/CT in newly diagnosed multiple myeloma patients: Comparison of volume-based PET biomarkers. Cancers (Basel) 2020, MDPI; 12:1042.
42. Ulaner GA, Sobol NB, O'Donoghue JA, Kirov AS, Riedl CC, Min R, et al. CD38-targeted immuno-PET of multiple myeloma: from xenograft models to first-in-human imaging. Radiology 2020;295:606–15.
43. Philipp-Abbrederis K, Herrmann K, Knop S, Schottelius M, Eiber M, Lückerath K, et al. In vivo molecular imaging of chemokine receptor CXCR4 expression in patients with advanced multiple myeloma. EMBO Mol Med 2015;7:477–87.
44. Shi L, Chen B, Liu T, Li L, Hu B, Li C, et al. ^{99m}Tc-CD3813: a nanobody-based single photon emission computed tomography radiotracer with clinical potential for myeloma imaging and evaluation of CD38 expression. Mol Pharm 2022;19:2583–94.
45. Bailly C, Gouard S, Lacombe M, Remaud-Le Saëc P, Chalopin B, Bourgeois M, et al. Comparison of immuno-PET of CD138 and PET imaging with $^{64}CuCl_2$ and [^{18}F]-FDG in a preclinical syngeneic model of multiple myeloma. Oncotarget 2018;9:9061–72.
46. Hallström UMFL. Proteomics. Tissue-based map of the human proteome. Science (1979) 2015;3476220:25613900.
47. Moreno L, Zabaleta A, Alignani D, Ajona D, Lasa M, Maiso P, et al. Critical analysis on the mechanism of action (MoA) of the anti-CD38 monoclonal antibody isatuximab in multiple myeloma (MM). Blood 2016;128:2105.
48. Morandi F, Horenstein AL, Costa F, Giuliani N, Pistoia V, Malavasi F. CD38: a target for immunotherapeutic approaches in multiple myeloma. Front Immunol 2018;9:2722.
49. Bruins WSC, Zweegman S, Mutis T, Van de Donk NWCJ. Targeted therapy with immunoconjugates for multiple myeloma. Front Immunol 2020;11:1155.
50. Larson SM, Carrasquillo JA, Cheung N-KV, Press OW. Radioimmunotherapy of human tumours. Nat Rev Cancer 2015;15:347–60.
51. Baidoo KE, Yong K, Brechbiel MW. Molecular pathways: targeted α-particle radiation therapy. Clin Cancer Res 2013;19:530–7.
52. De Vincentis G, Gerritsen W, Gschwend JE, Hacker M, Lewington V, O'Sullivan JM, et al. Advances in targeted alpha therapy for prostate cancer. Ann Oncol 2019;30:1728–39.
53. Jurcic JG, Rosenblat TL. Targeted alpha-particle immunotherapy for acute myeloid leukemia. American Society of Clinical Oncology Educational Book 2014;34:E126–31.
54. Pallares RM, Abergel RJ. Development of radiopharmaceuticals for targeted alpha therapy: where do we stand? Front Med 2022;9:1020188.
55. Nijhof IS, Casneuf T, Van Velzen J, van Kessel B, Axel AE, Syed K, et al. CD38 expression and complement inhibitors affect response and resistance to daratumumab therapy in myeloma. Blood 2016;128:959–70.
56. Tranel J, Feng FY, St James S, Hope TA. Effect of microdistribution of alpha and beta-emitters in targeted radionuclide therapies on delivered absorbed dose in a GATE model of bone marrow. Phys Med Biol 2021;66:035016.
57. VanWyngarden M, Walker Z, Su Y, Bearrows S, Stevens B, Forsberg P, et al. CD46 antibody drug conjugate impedes myeloma engraftment in patient-derived xenografts. Clin Lymphoma Myeloma Leuk 2019;19:E151.
58. Envigo. Comparative model radiosensitivity of immunodeficient mice in oncology studies [Internet]. Available from: Envigo. Radiosensitivity of immunodeficient mice in oncology studies. https://insights.envigo.com/hubfs/resources/white-papers/r2g2-mouse-comparative-model-radiosensitivity-white-paper.pdf.
59. Bobba K, Bidkar A, Wang S, Bidlingmaier S, Tang R, Su Y, et al. Influence of short PEG linkers on biodistribution of ^{225}Ac-Macropa-YS5, an immunoconjugate for treating CD46 expressing cancer. Nucl Med Biol 2022;108:S53.
60. Bobba KN, Bidkar AP, Meher N, Fong C, Wadhwa A, Dhrona S, et al. Evaluation of ^{134}Ce/^{134}La as a PET imaging theranostic pair for ^{225}Ac α-radiotherapeutics. J Nucl Med 2023;64:1076–82.